LAWRENCE
LIVERMORE
NATIONAL
LABORATORY

LLNL-JRNL-780620

Towards Predicting Removal Rate & Surface Roughness During Grinding of Optical Materials

T. Suratwala, R. Steele, L. Wong, P. Miller, E. Feigenbaum, N. Shen, N. Ray, M. Feit

July 8, 2019

Towards predicting removal rate & surface roughness during grinding of optical materials

Disclaimer

Towards predicting removal rate & surface roughness during grinding of optical materials

TAYYAB SURATWALA*, RUSTY STEELE, LANA WONG, PHIL MILLER, EYAL FEIGENBAUM, NAN SHEN, NATHAN RAY, AND MICHAEL FEIT

Lawrence Livermore National Laboratory, P.O. Box 808, Livermore, CA 94551, USA
**Corresponding author: suratwala1@llnl.gov* LLNL-JRNL-780620

Received XX Month XXXX; revised XX Month, XXXX; accepted XX Month XXXX; posted XX Month XXXX (Doc. ID XXXXX); published XX Month XXXX

A series of controlled grinding experiments, utilizing loose or fixed abrasives of either alumina or diamond at various particle sizes, were performed on a wide range of optical workpiece materials [single crystals of Al_2O_3 (sapphire), SiC, $Y_3Al_5O_{12}$ (YAG), CaF_2, and LiB_3O_5 (LBO); a SiO_2-Al_2O_3-P_2O_5-Li_2O glass ceramic (Zerodur); and glasses of SiO_2:TiO_2 (ULE), SiO_2 (fused silica), and P_2O_5-Al_2O_3-K_2O-BaO (Phosphate)]. The material removal rate, surface roughness, and the morphology of surface fractures were measured. Separately, Vickers indentation was performed on the workpieces, and the depths of various crack types as a function of applied load was measured. Single pass grinding experiments showed distinct differences in the spatial pattern of surface fracturing between the loose alumina abrasive (isolated indent-type lateral cracking) and the loose or fixed diamond abrasive (scratch-type elongated lateral cracking). Each of the grinding methods had a removal rate and roughness that scaled with the lateral crack slope, s_ℓ (i.e. the rate of increase in lateral crack depth with the applied load) of the workpiece material. A grinding model (based on the volumetric removal of lateral cracks accounting for neighboring lateral crack removal efficiency and the fraction of abrasive particles leading to fracture initiation) and a roughness model (based on the depth of lateral cracks or the interface gap between the workpiece and lap) are shown to quantitatively describe the material removal rate and roughness as a function of workpiece material, abrasive size, applied pressure and relative velocity. This broad, multi-process variable grinding model can serve as a predictive tool for estimating grinding rates and surface roughness for various grinding processes on different workpiece materials.

OCIS codes: (220.4610) Optical fabrication; (350.3850) Materials processing; (160.2750) Glass and other amorphous materials; (160.4670) Optical materials; (160.6030) Silica

http://dx.doi.org/10.1364/AO.99.099999

1. INTRODUCTION

The grinding of brittle materials can be described microscopically as the removal of workpiece particles created from an ensemble of single or intersecting brittle fractures, which are caused by an ensemble of normally loaded, hard indenters or abrasives sliding or rolling across the surface of the workpiece. Analogous to the Preston equation for polishing, the macroscopic grinding material removal rate can be described as:

$$\frac{dh}{dt} = k_p \sigma_o V_r \qquad (1)$$

where dh/dt is the average thickness removal rate, k_p is the grinding Preston coefficient, σ_o is applied pressure, and V_r is the average relative velocity of the abrasive relative to the workpiece. The grinding Preston coefficient incorporates many process parameters related to: the grinding particle (material properties, particle size distribution and shape); the lap or tool (material properties); the workpiece (material properties); and the contact conditions (lubricant, temperature, friction). Owing to the complex nature of all these interactions, a single integrated model, starting from fundamental fracture mechanics, which predicts the material removal rate as a function of the combined process and material parameters has proven elusive [1].

To date, two general strategies for developing grinding models have been utilized: 1) statistical grinding models, requiring the determination of empirical parameters experimentally, or 2) figure-of-merit models, providing useful relative correlations of fracture behavior of the workpiece materials. One example for the first strategy is using a breaking function from Poisson statistics which set the basis for predicting the material removal rate for various grinding conditions [2, 3]. Another approach using this strategy involves measuring the spatial and temporal dependence of the crack distribution on the workpiece which was then used to determine the material removal rate using a modified Preston-equation approach [4]. Such approaches, however, require experimental measurements to determine parameters describing the crack distribution for each grinding system.

In the second strategy, the influence of workpiece mechanical properties on the grinding rate ~~have~~ has been characterized which establish material removal figure-of-merits (FOMs) by comparing the grinding rates of many glasses processed under a standardized, fixed grinding process. Aleinikov [5], Izumitani [6, 7], Buijs [8], and Lampropoulus [9] correlated these grinding FOMs to basic indentation crack-growth behavior, ultimately giving rise to the term lapping hardness (LH). Lapping hardness is derived from the principle that the volume of material removed is dominated by chips removed from the workpiece, that are created by lateral cracks from mechanically loaded abrasives sliding across the workpiece [9]. Hence the contribution of the workpiece material properties to the grinding Preston coefficient should scale with the lapping hardness (*LH*), which is defined as:

$$LH = \frac{E_1^{7/6}}{K_{Ic}H_1^{23/12}} \sim \frac{E_1}{K_{Ic}H_1^2} \quad (2)$$

where E_1 is the workpiece elastic modulus (GPa), K_{1c} is the workpiece fracture toughness (MPa $m^{0.5}$), and H_1 is the workpiece Knoop hardness (GPa). In addition to material removal rate, the depth of lateral crack and the height of the plastic zone were also utilized as a metric to describe the workpiece surface roughness [1, 10, 11].

In the following study, we expand the lateral crack concept previously utilized for grinding material removal rate and roughness, for both fixed and loose abrasive grinding for a wide variety of optical materials. Validated by grinding data, an expanded grinding model is presented which utilizes: 1) volumetric lateral crack removal, accounting for the removal efficiency of neighboring lateral cracks and the fraction of abrasive particles loaded, to describe material removal rate; and 2) lateral crack depth or interface gap to describe the workpiece surface roughness. Also, the resulting grinding model not only applies to lateral crack growth properties of the workpiece, but also to important grinding parameters, such as abrasive particle size, applied pressure and kinematics (i.e. relative velocity).

2. EXPERIMENTAL

Optical material workpieces. Nine different optical workpiece materials were utilized for the indentation and grinding experiments: single crystal Al_2O_3 (Sapphire) (a-plane, Coastline Optics, Camarillo, CA), single crystal SiC (SiC-6H 0001, MTI Corporation, Richmond, CA), single crystal $Y_3Al_5O_{12}$ (YAG) (Northrop Grumman/Synoptics, Charlotte, NC), single crystal CaF_2 (111 orientation, ISP, Irvington, NY), single crystal LiB_3O_5 (LBO) (2ω doubler cut, Coherent Crystal, New Jersey), SiO_2-Al_2O_3-P_2O_5-Li_2O glass ceramic (Zerodur) (Schott, Duryea, PA), SiO_2:TiO_2 glass (ULE) (Corning Inc., Corning, NY), SiO_2 glass (Fused Silica) (Corning 7980, Corning Inc., Corning, NY), and P_2O_5-Al_2O_3-K_2O-BaO glass (Phosphate glass) (LHG-8, Hoya Corporation, Milpitas, CA). All the samples were 50 mm in diam and typically 1 cm thick.

Indentation experiments. Vickers indentation was performed on a polished surface of each of the workpiece materials in air at room temperature using an indenter (HMV Micro Hardness Tester, Shimadzu) with a loading rate of 0.2 cm/sec. 10 indents were applied at 9 different peak loads (ranging from 0.098N to 19.6N) on each of the workpiece materials (i.e., 90 indents on each workpiece). The radial and lateral crack depths (i.e., the deepest part of that crack type) were measured for each indent for each load-workpiece combination, and the average value was reported.

Grinding experiments. Loose abrasive grinding of each of the workpiece materials was conducted on a 300 mm diameter granite lap utilizing Al_2O_3 abrasives (Microgrit WCA 9T, 15T and 30T; Universal Photonics, Hicksville, NY) or diamond abrasives (DMS poly 8-12 K285T, Sandvik Hyperion, Worthington, OH). The loose abrasive slurries were prepared as 5 parts water to 1 part abrasive powder and fed single pass with a 1.2 mL/min feed rate using a peristaltic pump.

Fixed abrasive grinding was performed using diamond abrasives in a resin bond (3M™ Trizact™ diamond tile abrasive pad; 9 μm, 20 μm, and 45 μm) adhered to a 300 mm granite lap utilizing a water feed rate of 1.2 mL/min. Each of the fixed abrasive pads were pre-treated with an Al_2O_3 grinding disk (0.5 psi for ~5 min) to ensure the fixed diamond abrasives were exposed on the surface.

The same grinding conditions for both the loose and fixed abrasive were utilized for each of the workpiece materials (unless otherwise specified): lap rotation=20 rpm, workpiece rotation=20 rpm, center offset between workpiece and lap center of 75 mm, applied pressure on workpiece of 1.1 psi using weights on the workpiece. The grinding material removal rate was measured gravimetrically. Depending on the observed material removal rate, the grinding times were adjusted between 3 to 180 min to ensure sufficient removal for an accurate mass removal measurement. Each grinding slurry-workpiece combination was repeated for 3-5 iterations for the loose abrasive and for 10 iterations for the fixed abrasive, and the average material removal rate was reported. The surface roughness for each of the ground workpieces was measured using needle profilometry (AlphaStep D-100, KLA-Tencor, Milpitas, CA) using the following conditions: scan length=10 mm, stylus force=1 mgf, and a scan speed=0.15 mm/s.

Single pass grinding experiments. Starting with polished surfaces of fused silica, these workpieces were slid once under a load of 1.1 psi across a 1 cm track containing various 9 μm abrasives described above (loose Al_2O_3, loose diamond, and fixed diamond) on a granite lap. The workpieces were then characterized using optical microscopy before and after chemical etching of 1 μm using 6:1 buffered oxide etch ($HF:NH_4F$) 3x diluted in de-ionized water to evaluate the nature and distribution of the surface fractures generated.

3. RESULTS

The relationships that govern the extent of the radial and lateral fractures, in isotropic materials following crack initiation, as a function of applied load (P) generally scale as [12-14]:

$$c_r = s_r P^{2/3}$$
$$c_\ell = s_\ell P^{1/2} \quad (3a\text{-}c)$$
$$b_\ell = s_{\ell b} P^{5/8}$$

where c_r and c_ℓ are the crack depths (μm), and b_ℓ is the crack length (μm). The subscripts r and ℓ designate radial ~~or~~ and lateral cracks, respectively. Fig. 1 shows example microscope images of the Vickers indents on the various workpiece materials at two selected loads (1.96 N and 19.6 N). The corresponding measured radial and lateral crack depths as a function of the scaled load are shown in Fig. 2. The slopes of the curves in the Figure are referred to as the radial crack slope, s_r and the lateral crack slope, s_ℓ. The determined values of the crack slopes (s_r and s_ℓ) for each of the workpiece materials along with some relevant material properties (literature values) are shown in Table 1.

It has been previously reported that the crack slopes scale nominally with $(E_1/H_1K_{Ic}^2)^{1/3}$ for radial cracks and $E_1^{1/2}/H_1$ for lateral cracks [9, 12]. ~~This~~ These correlations ~~is~~ are largely valid, as illustrated in Fig. 3 (using values shown in Table 1), even for the broad range of workpiece materials evaluated in the present study (i.e., glasses versus glass ceramics versus single crystals; oxides versus fluorides versus carbides). Hence, when the crack slopes for a given workpiece material are not readily available, they can typically be estimated using the basic material properties of the workpiece as:

$$s_r \approx \text{~~0.077~~}7.7\left(\frac{E_1}{H_1K_{Ic}^2}\right)^{\frac{1}{3}} - 6.5 \quad (4\text{~~)~~})$$

$$s_\ell \approx 17.8\frac{\sqrt{E_1}}{H_1} - 15.5 \quad (5)$$

where s_r is in units of μm/$N^{2/3}$ and s_ℓ is in μm/$N^{1/2}$ when E_1 and H_1 are in GPa and K_{Ic} is in MPa $m^{1/2}$. Also, from the same indentation experiments shown in Fig. 1, the lateral crack length b_ℓ was largely proportional to the lateral crack depth c_ℓ. Hence, despite the slightly different load dependencies (compare Equation 3b with 3c), the lateral crack length slope, $s_{\ell b}$, is approximated as $s_{\ell b} \approx 17 s_\ell$. For simplicity, the grinding correlations presented in the remainder of the discussion are described in terms of the measured crack slopes shown in Table 1.

Some of the glasses use in this study known densify upon loading, such as fused silica and ULE, are referred to as anomalous glasses.[15]

Since depths of the lateral and radial cracks were measured directly, instead of indentation and plastic zone, the effects of densification are accounted for in the measured lateral crack slopes in Table 1.

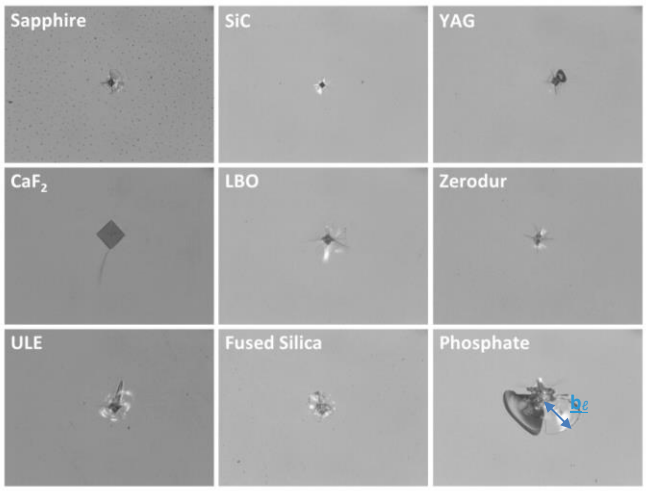

(a)

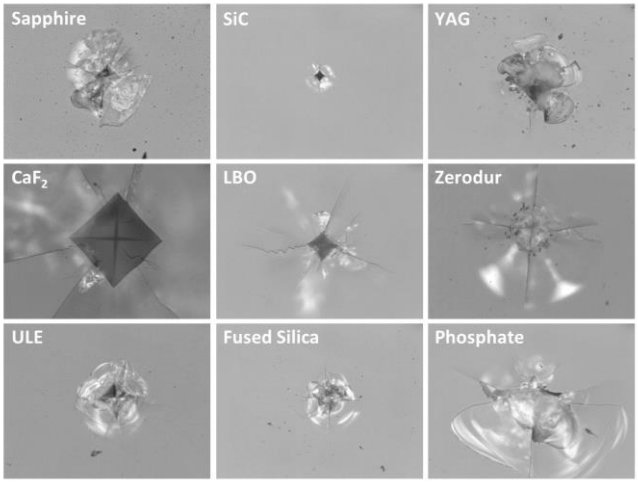

(b)

Fig. 1. Examples of observed Vickers indent fractures observed on various optical workpiece materials at (a) 1.96 N and (b) 19.6 N applied loads. Each microscope image is 338 μm x 254 μm.

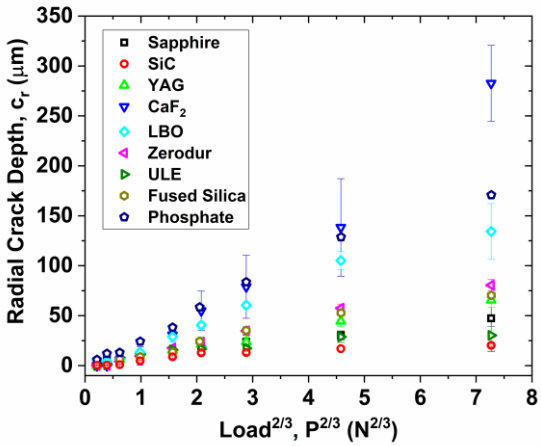

(a)

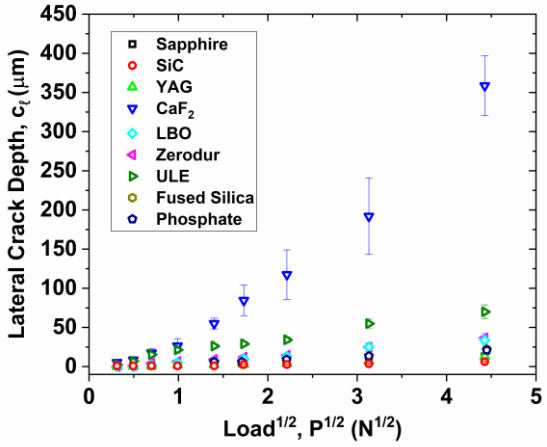

(b)

Fig. 2. (a) Radial crack depth (c_r) and (b) lateral crack depth (c_ℓ) as a function of scaled applied load for various optical workpiece materials.

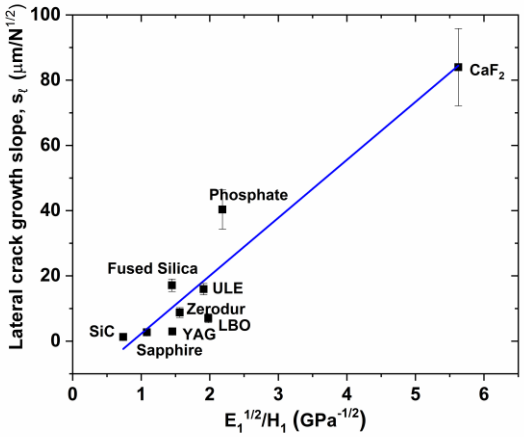

(a)

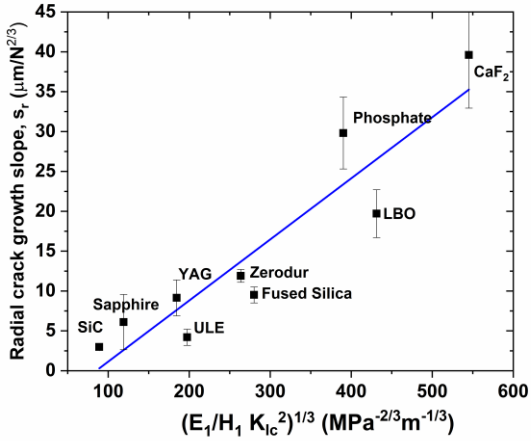

(b)

Fig. 3. Correlation between the (a) radial and (b) lateral crack growth slope as a function of proposed workpiece material property scaling factor.

Table 1. List of workpiece materials, basic material properties (literature values), and ~~determined~~ lateral and radial crack growth slopes (determined from the indentation experiments).

Workpiece Material	Material Type	Material Properties*			Crack Properties	
		Young's modulus, E_1	Knoop hardness, H_1	Fracture toughness, K_{Ic}	Lateral crack depth slope, s_ℓ	Radial crack depth slope, s_r
		GPa	GPa	MPa·m$^{0.5}$	μm/N$^{1/2}$	μm/N$^{2/3}$
Sapphire (Al_2O_3)	single crystal	345	~~3.4~~17.2	3.45	2.~~76~~9 ±0.6	6.1 ±3.5
Silicon Carbide (SiC)	single crystal	410	27.~~54.0~~	4.6	1.~~32~~8 ±0.2	~~2.98~~3.0 ±0.2
YAG ($Y_3Al_5O_{12}$)	single crystal	300	~~2.9~~11.9	2	3.0~~2.96~~ ±0.8	9.1~~4~~ ±2.2
Calcium Fluoride (CaF_2)	single crystal	76	~~0.7~~1.5	0.55	84.0 ±11.8	39.~~639~~.~~6~~ ±6.6
LBO (LiB_3O_5)	single crystal	140	~~1.4~~6.0	0.54	7.0~~2~~ ±1.4	19.7 ±3.0
Zerodur (SiO_2:Al_2O_3:P_2O_5:Li_2O)	glass-ceramic	90.3	~~0.9~~6.1	0.9	8.~~87~~6 ±1.5	11.9 ±0.8
ULE (SiO_2:TiO_2)	glass	68	4.~~30.7~~	1.43	15.~~9.59~~4 ±1.8	4.2 ±1.0
Fused Silica (SiO_2)	glass	72.7	5.~~90.7~~	0.75	17.1 ±1.9	9.5~~1~~ ±1.0
Phosphate (P_2O_5-Al_2O_3-K_2O-BaO)	glass	50	3.~~20.5~~	0.51	40.3 ±6.0	29.8 ±4.5

*for anisotropic crystals, average material property value reported

Fig. 4 shows SEM images of the abrasives used this study. The loose alumina particles (Microgrit) are known to have a largely blunt, plate-like morphology (see Figs. 4a-c), whereas both the loose and fixed diamond particles have a sharp character to them (see Figs. 4d-f).

Fig. 5 shows optical micrographs of the single slide grind of the fused silica workpiece surfaces before and after a short chemical etch to reveal all the surface cracks. Two key parameters were evaluated with respect to crack morphology for this experiment: 1) the difference between blunt alumina particles versus the sharper diamond particles; and 2) the difference between loose (3-body) and fixed (2-body) abrasive processes. Comparing Fig. 5a with 5b-c, the nature of the cracks generated ~~are~~ is very different for the loose abrasive alumina particles. The fracturing appears largely as isolated indents, creating both trailing indent type cracks [16, 17] and isolated lateral cracks, similar to that observed by static indentation. In contrast, the fracturing with the diamond particles (loose or fixed), have a more linear scratch behavior where the trailing indent and lateral fractures line up with the scratch direction. The fact that both the loose and fixed diamond particles have similar fracturing behavior, it is likely that the sharpness and/or hardness of the abrasive particles are driving the observed fracturing behavior, as opposed to the loose (3-body) versus fixed (2-body) constraints. Previous studies, which evaluated the character of scratches, showed similar morphologies. A blunt particle led to trailing indent and lateral cracks, and a sharp particle led to a linear plastic trench following the particle path with accompanying trailing indent fractures and side lateral fractures [16, 17].

The grinding rate and roughness results are summarized in Figs. 6-8 for the various abrasives; the data is presented as a function of lateral crack growth slope s_ℓ of a given workpiece material. Regardless of the abrasive characteristic (alumina versus diamond; loose versus fixed; or abrasive size), both the removal rate and roughness were observed to increase with the lateral crack slope. This indicates the importance of the lateral crack properties of the workpiece on these grinding characteristics, as implied by previous work. Also, regardless of abrasive type, the removal rate and roughness increased with abrasive size.

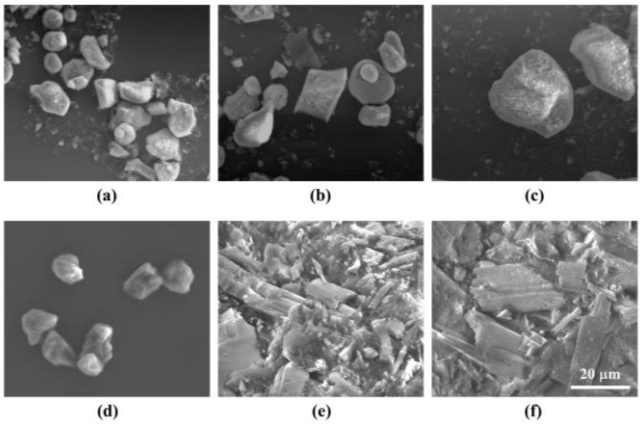

Fig. 4. SEM images of various abrasives used for grinding: (a) 9 μm Alumina loose abrasive; (b) 15 μm Alumina loose abrasive; (c) ~~45~~30 μm Alumina loose abrasive; (d) 10 μm diamond loose abrasive, (e) 20 μm diamond fixed abrasive, and (f) 45 μm diamond fixed abrasive.

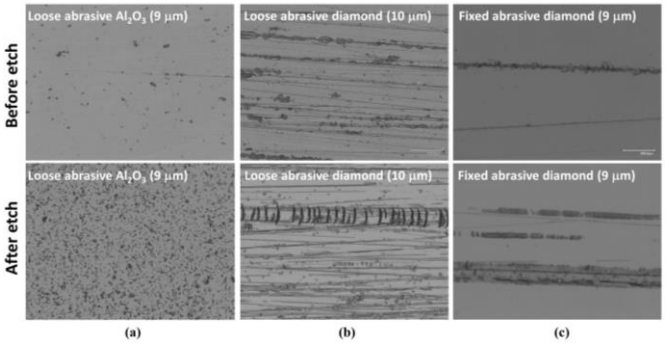

Fig. 5. Optical micrographs of fused silica surface after single pass grind from left to right using various abrasives (loose abrasive alumina, loose abrasive diamond, fixed abrasive diamond) both before and after etching. Each microscope image is 501 μm x 670 μm.

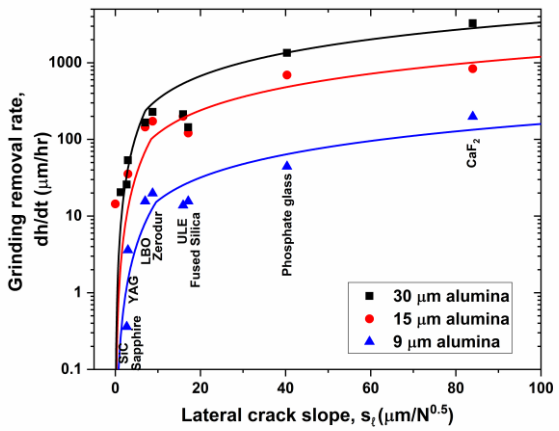

(a)

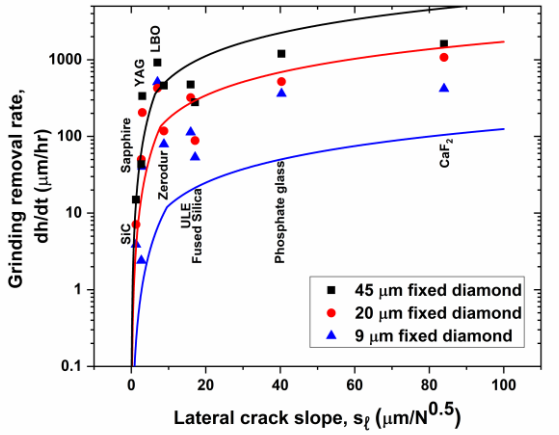

(b)

Fig. 6. Grinding rate of various workpiece materials as a function of the lateral crack slope (s_ℓ) using (a) alumina loose abrasive grinding at various particle sizes and (b) diamond fixed abrasive grinding at various particle sizes. The lines represent the lateral crack grinding rate model (Equation 13).

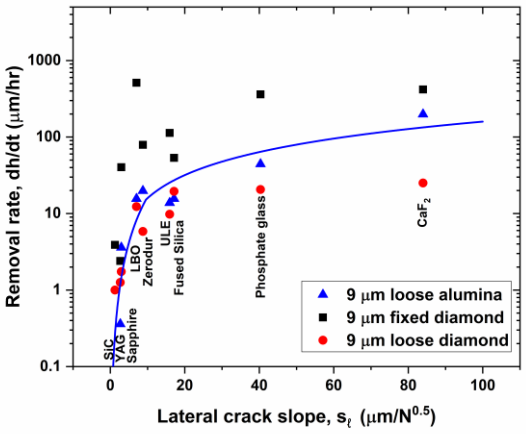

Fig. 7. Grinding rate of various workpiece materials as a function of the lateral crack slope (s_ℓ) using various types of ~9 μm abrasives. The line represents the lateral crack grinding rate model (Equation 13).

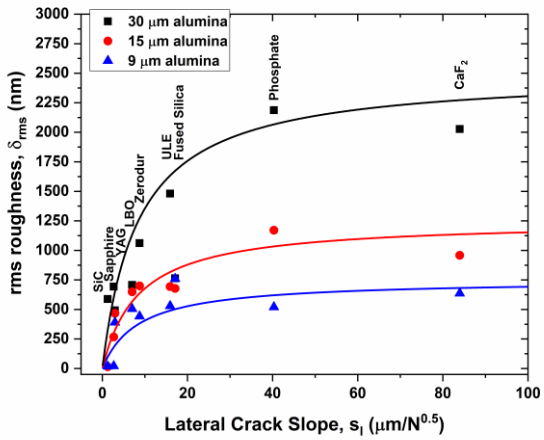

(a)

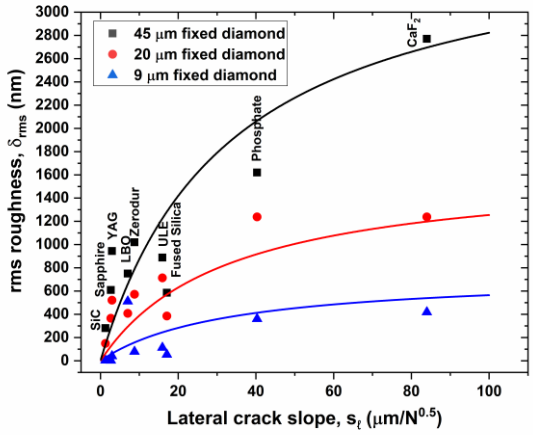

(b)

Fig. 8. Surface roughness of various workpiece materials as a function of the lateral crack slope (s_ℓ) for (a) alumina loose abrasive grinding at various particle sizes and (b) diamond fixed abrasive grinding at various particle sizes. The lines represent the surface roughness model (using Equation 15 with c_g=6 & c=1.6 for the loose abrasive grind and c_g=6 & c=0.4 for the fixed abrasive grind).

4. DISCUSSION

As discussed in the Introduction, the mechanical loading of abrasive particles leading to the generation of surface cracks, together with the mechanism of fracture, are the determining factors for material removal and surface roughness during grinding. As proposed by Lambropolous and others, lateral cracks are the dominant crack type determining the characteristics of grinding [9]. As presented in the Results Section, the lateral crack slope (s_ℓ) is a good indicator of both the grinding rate (Figs. 6-7) and the grinding roughness (Fig. 8) for a large range of workpiece materials and for a large range in grinding process parameters (abrasive material and shape, loose versus fixed abrasive, and abrasive size). Workpieces with a larger lateral crack slope generate larger lateral cracks for the same grinding conditions. This leads to: 1) greater volumetric glass removal and hence higher thickness material removal rate; and 2) deeper exposed surface fractures and hence larger surface roughness. Similarly, grinding with larger abrasives leads to a larger average load per particle [18], hence leading to larger lateral cracks (as given by Equations 3b-c) and larger removal rates and surface roughness.

In the discussion that follows, these concepts are expanded to provide a generalized predictive grinding model describing removal rate (*Section A*) and surface roughness (*Section B*) as a function of both workpiece materials properties (namely s_ℓ) and the important, dominant grinding process parameters (such as abrasive size, applied pressure, and relative velocity).

A. Grinding Removal Rate

1. Model Setup

This treatment describes the geometry of single lateral crack as a simple rectangular cuboid with depth c_ℓ, length b_ℓ, and width $2r$ (where r is the radius of the abrasive particle) (see Fig. 9). The thickness removal rate, based on the volumetric removal of lateral cracks, can be described in the following form:

$$\frac{dh}{dt} = f_{Lf}(r)\, I(s_\ell, r)\, c_\ell b_\ell 2r \frac{V_r}{d_s} N_t \qquad (6)$$

where $f_{Lf}(r)$ is the fraction of loaded particles that are leading to fracture, I is the efficiency of volumetric removal of two neighboring cracks, V_r is the particle velocity relative to the workpiece surface (μm/s), d_s is the spacing between created lateral cracks generated by the abrasives (μm), and N_t is the areal density of loaded particles (μm^{-2}). Note $c_\ell b_\ell 2r$ is the volume of a single lateral crack (μm^3), and V_r/d_s is the rate of creation of lateral cracks by a single particle (s^{-1}).

The average load per particle (P) can be described as:

$$P = \frac{\sigma_o}{N_t} \qquad (7)$$

where N_t is given by:

$$N_t = \frac{f f_L}{\pi r^2} \qquad (8)$$

and where f is the areal fill fraction of particles at the interface between workpiece and lap, and f_L is the fraction of particles loaded. A reasonable value for the fill fraction f for a set of random particles is 0.3.

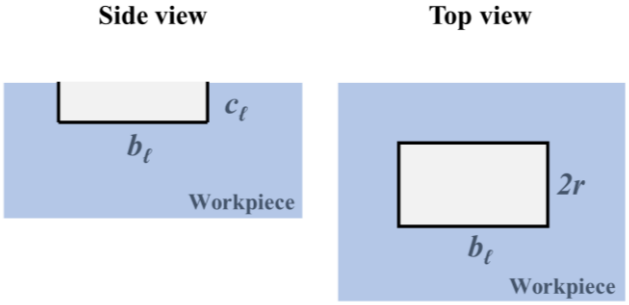

Fig. 9. Geometry of lateral cracks utilized in grinding model; rectangular cuboid with depth c_ℓ, length b_ℓ, and width $2r$ (where r is the radius of the abrasive particle).

As analyzed in our previous grinding study, if all the particles at the interface were mechanically loaded, the load per particle would be orders-of-magnitude too low to lead to fracture [18]. Hence the fraction of particles in the interface that are under load is quite small. From the single pass grind experiments (e.g., see Fig. 5), the average length of the lateral cracks was measured for both the 9 μm and 30 μm loose abrasive (see Table 2). Then using Equation 3c, the average load per particle (P) can be estimated, and using Equations 7&8, the fraction of loaded particles can be estimated as f_L~5x10^{-4} (again see Table 2).

Table 2. Determined load per particle from single pass grinding compared with the load per particles using f_L=5x10^{-4}.

Parameter	9μm loose abrasive	30 μm loose abrasive
Average lateral crack length (b_ℓ)	5.0 μm	11.4 μm
Calculated load per particle using Equation 3c (P)	0.0038 N	0.014 N
Calculated load per particle (P) assuming f_L=5x10^{-4} using Equations 7 & 8	0.0032 N	0.036 N

Substituting Equations 3b-c, 7, & 8 into Equation 6, the material removal rate now takes the form:

$$\frac{dh}{dt} = f_{Lf}(r)\, I(s_\ell, r) s_\ell s_{lb} \left(\frac{\pi}{f_{Lf}}\right)^{1/8} \left(\frac{2}{d_s}\right) r^{5/4} {\sigma_o}^{9/8} V_r \qquad (9)$$

What remains in order to have a more useful form of the material removal rate expression are quantitative descriptions of the fraction of loaded particles leading to fracture ($f_{Lf}(r)$) and the volumetric removal efficiency of neighboring cracks ($I(s_\ell, r)$). Each of these is described below.

2. Fraction of loaded particles leading to fracture

The fraction of loaded particles leading to fracture influences the overall removal rate via the number of lateral fractures created, as opposed to the volume of a single lateral crack. At the workpiece-lap interface, using the Hertzian contact mechanics, there will be a load per particle distribution largely driven by the particle size distribution of the abrasive [18]. In our previous grinding study, the load on a given particle was found to be linearly proportional to the size of the particle [18]. Also, it has been shown that only the largest particles in the workpiece-lap interface are load bearing whether during grinding or polishing [16, 18, 19]. In addition, for most abrasives, the tail end of the particle size distribution representing the largest particles can be described by a single exponential [18].

Hence the cumulative load per particle distribution F_L can be described in the form:

$$F_L = 1 - exp\left(\frac{P_i}{P}\right) = 1 - exp\left(\frac{P_i}{\frac{\sigma_o \pi r^2}{f_{Lf}}}\right) \qquad (10)$$

where P_i is the mechanical load on particle i, and P is the average load per particle. Fig. 10a shows the calculated load per particle distribution for the three different abrasive sizes using Equation 10. There is a critical load (P_c) required before a lateral crack can initiate. Sliding indentation with friction has been shown to have initiation loads <<0.1 N; here we chose P_c =0.0073 N [12, 20]. Incorporating P_c into Equation 10, the fraction of loaded particles leading to fracture ($f_{Lf}(r)$) is then given by:

$$f_{Lf}(r) = exp\left(\frac{-P_c}{\frac{\sigma_o \pi r^2}{f_{Lf}}}\right) \qquad (11)$$

Fig. 10b shows the calculated fraction of loaded particles leading to fracture as calculated by Equation 11 for the parameters evaluated in this study (σ_o=1.1 psi, f_L=5x10^{-4}, and P_c=0.00735 N).

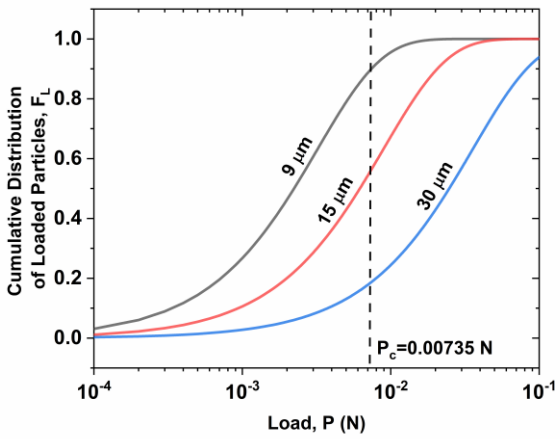

(a)

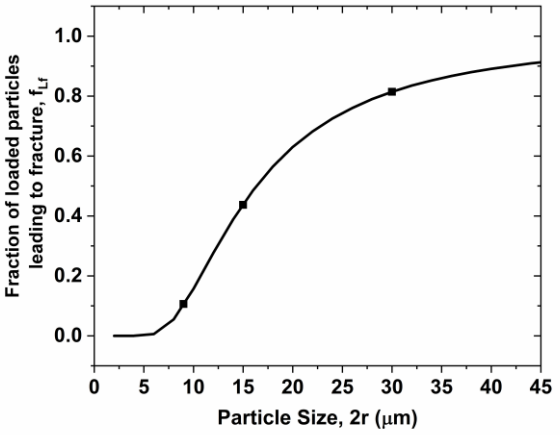

(b)

Fig. 10. (a) Calculated load per particle cumulative distribution F_L for different abrasive sizes using Equation 10 with σ_o=1.1 psi and f_L=5x10^{-4}. The vertical dashed line represents P_c=0.00735 N. (b) Calculated fraction of loaded particles leading to fracture $f_{Lf}(r)$ for different abrasive sizes using Equation 11 with σ_o=1.1 psi, f_L=5x10^{-4}, and P_c=0.00735 N.

3. Efficiency of Volumetric removal by neighboring lateral cracks

The efficiency of volumetric removal (I) accounts for the decrease in removal volume when neighboring lateral cracks start to intersect with each other. When lateral cracks are spaced far apart (which occurs more often with small lateral cracks or workpiece materials with small values of s_ℓ), the volumetric efficiency of removal is 1 or 100%. When lateral cracks overlap (which occurs more often with large lateral cracks or workpiece materials with larger values of s_ℓ) its volumetric removal efficiency decreases.

The relative spacing between lateral cracks will determine its efficiency of volumetric removal [21]. This concept is illustrated in Fig. 11a. Consider radial and lateral cracks whose fracture initiations have a final equilibrium spacing of d_{sf}. If the lateral crack length b_ℓ is less than half of the distance d_{sf}, then the removal efficiency would be I=1. In other words, lateral cracks do not overlap. If the ratio b_ℓ/d_{sf}>0.5, then the efficiency of removal will decrease with a value of $I=d_{sf}/2b_\ell$. Using Equations 3c, 7 & 8, the efficiency of volumetric removal can be written as a function of s_ℓ and r as:

$$I(s_\ell, r) = 1 \qquad if \ \frac{17 s_\ell \left(\frac{\sigma_o \pi r^2}{f_{Lf}}\right)^{5/8}}{2r} \le 0.5 \qquad (12a)$$

$$I(s_\ell, r) = \frac{r}{17 s_\ell \left(\frac{\sigma_o \pi r^2}{f_{Lf}}\right)^{5/8}} \qquad if \ \frac{17 s_\ell \left(\frac{\sigma_o \pi r^2}{f_{Lf}}\right)^{5/8}}{2r} > 0.5 \qquad (12b)$$

This relationship assumes that final equilibrium spacing between lateral cracks is proportional to the abrasive size, namely d_{sf}=2r. Fig. 11b shows a plot of volumetric removal efficiency as function of the workpiece s_ℓ illustrating the large decrease in removal efficiency when lateral cracks increase in size. Note that the removal efficiency also decreases weakly with increase in abrasive size, scaling as $r^{-1/4}$ (see Equation 12b).

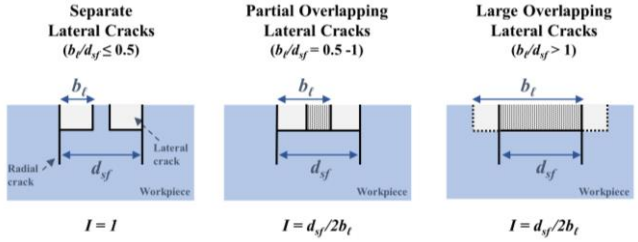

(a)

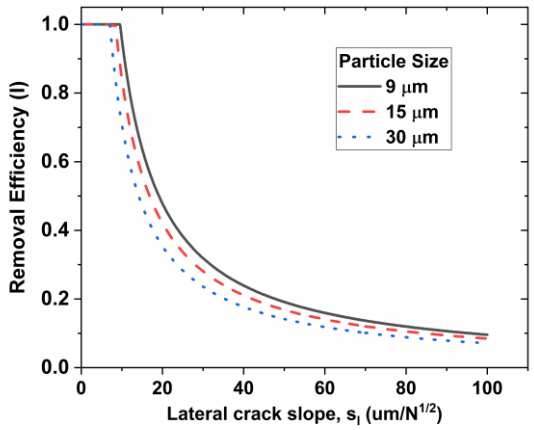

(b)

Fig. 11. (a) Schematic illustrating the change in volumetric removal efficiency (I) as a function of the degree of overlap of neighboring lateral cracks (b_ℓ/d_{sf}). (b) Calculated volumetric removal efficiency as a function of $I(s_l, r)$ and as a function of s_ℓ at different abrasive sizes using Equations 12a-b with σ_o=1.1 psi, f_L=5x10^{-4}, and f=0.3.

4. Grinding material removal rate expression & implications

The removal rate expression given by Equation 9 can now be rewritten incorporating Equation 11 (fraction of loaded particles leading to fracture) and Equation 12 (volumetric removal efficiency) in a more convenient analytical form as:

$$\frac{dh}{dt} = C_1 \, s_\ell \, r \, {\sigma_o}^{1/2} \, V_r \, exp\left(\frac{-C_2}{\sigma_o r}\right)$$

$$if \ C_4 s_\ell {\sigma_o}^{5/8} r^{1/4} > 0.5 \qquad (13a)$$

$$\frac{dh}{dt} = C_3 \, {s_\ell}^2 \, r^{\frac{5}{4}} \, \sigma_o^{\frac{9}{8}} \, V_r \, exp\left(\frac{-C_2}{\sigma_o r}\right)$$

$$if C_4 s_\ell {\sigma_o}^{5/8} r^{1/4} < 0.5 \qquad (13b)$$

where the removal rate is a function of the lateral crack slope (s_ℓ), abrasive size ($2r$), applied pressure (σ_0) and relative velocity (V_r). C_1, C_2, C_3 and C_4 are constants which are unique to the given grinding system. They are defined by some basic characteristics of the system discussed above as:

$$C_1 = \frac{2}{d_s}\sqrt{\frac{f_{Lf}}{\pi}} \qquad (13c)$$

$$C_2 = \frac{P_c f_{Lf}}{\pi} \qquad (13d)$$

$$C_3 = \frac{34\, N^{-1/8}}{d_s}\left(\frac{\pi}{f_{Lf}}\right)^{1/8} \qquad (13e)$$

$$C_4 = \frac{17\, N^{-1/8}}{2}\left(\frac{\pi}{f_{Lf}}\right)^{5/8} \qquad (13f)$$

The solid lines in Fig. 6a are the grinding model results (using Equation 13) compared with the experimentally measured grinding rate with the loose abrasive alumina. The model captures the lateral crack growth (i.e., workpiece) dependence and abrasive particle size dependence for the grinding rate quite well spanning almost five orders of magnitude. Also, this grinding model (Equation 13a-b) largely predicts similar pressure and relative velocity dependences (particularly in the second regime) as the global Preston Equation (Equation 1).

The model used determined values or process parameters or characteristics (applied pressure, σ_0=1.1 psi; relative velocity, V_r=15.7 cm/s; fraction of loaded particles, f_L=5x10^{-4}; fill fraction of particles at the interface, f=0.3; critical load to initiate fracture, P_{ct} =0.0073 N; and spacing between lateral cracks, d_s=250 μm). The corresponding values for the four constants are C_1=53.3 m^{-1}, C_2=3.51x10^{-7} N, C_3=4.72x10^5 N$^{-1/8}$m^{-1}, and C_4=4.27x10^3 N$^{-1/8}$.

The grinding rate behavior followed two regimes with s_ℓ. For workpiece materials with small s_ℓ, lateral cracks have little or no overlap resulting in 100% volumetric removal efficiency and a large increase in grinding rate with s_ℓ. For workpiece materials with large s_ℓ, lateral cracks have greater overlap reducing the efficiency of volumetric removal and hence a reduction in the rate of increase in grinding rate with s_ℓ.

In contrast to the loose abrasive alumina grinding results, the fixed abrasive diamond grinding results deviated significantly from the model (as shown Fig. 6b). The reason for this deviation is believed to be due to another important process variable that applies to fixed abrasive, but not to the loose abrasive, which has not been incorporated into the current model. This is the degree of and the rate of exposure of fixed diamonds to the surface either due to lap wear or buildup of workpiece products (often called 'swarf') at the interface. This phenomenon influences the number of diamond particles available to be loaded against the workpiece, hence the load per particle distribution during grinding, and ultimately the grinding removal rate.

To illustrate, the same fixed abrasive diamond process using the 20 μm diamond was conducted with a much more aggressive conditioning of the fixed abrasive lap (using an Al_2O_3 grinding disk) (see Fig. 12). The grinding rate increased significantly with the extra conditioning for the same set of workpiece materials. This result supports that the rate of exposure of fixed diamonds to the surface is an important factor influencing the grinding removal rate.

Expanding the current grinding model to include the effect of lap wear and swarf buildup for fixed abrasive grinding will lead to a more complex model whose removal rate is time dependent. Developing such a model is left for future studies. However, the grinding removal rate model in this study (Equation 13) quantitatively describes the removal rate for various workpieces and grinding parameters for loose abrasive grinding. It also captures important trends in the grinding removal rate for fixed abrasive grinding ~~as well~~.

B. Grinding Roughness

As described by Lambropoulos [10], the surface roughness of the workpiece after grinding is likely related to the depth of the lateral crack generated on that workpiece. Qualitatively, the data from this study is consistent with this concept, where the workpiece surface roughness after grinding increases with the lateral crack slope and with the abrasive particle size for various types of grinding processes (both of which would increase the load per particle and depth of lateral cracks) (see Figs. 8a-b).

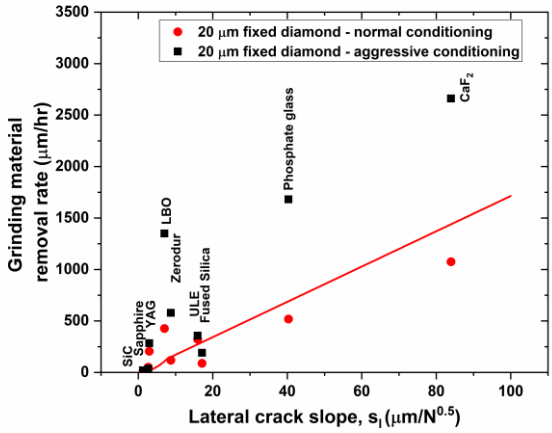

Fig. 12. Comparison of 20 μm diamond fixed abrasive grinding for various workpiece materials as a function of the lateral crack slope and degree of the lap conditioning.

However, for a workpiece material with a large lateral crack slope, the roughness appears to plateau. That is, use of a series of substrate materials with successively larger lateral crack slopes does not necessarily result in increased roughness (see Figs. 8a-b). As shown in these figures for a given abrasive size, surface roughness becomes largely independent of material, provided that the material has a sufficiently large lateral crack slope. This suggests that surface roughness is not exclusively determined by lateral crack depth. We suggest that this plateau results as the depth of the lateral crack approaches the dimension of the interfacial gap between the workpiece and the lap. As shown in Fig. 13, owing to geometric considerations, the depth of the lateral cracks cannot exceed the workpiece-lap interface gap. Note, that the use of larger abrasive particles leads to larger interfacial dimensions, thus the plateau roughness is found to increase. This trend was observed in the data in Figs. 8a-b, where the plateau roughness increases with abrasive size, consistent with the interface gap concept.

A simple roughness model can account for both of these effects, where the rms roughness would be described as:

$$\delta_{rms} = \left(\frac{1}{c\, c_\ell} + \frac{1}{\frac{r}{c_g}}\right)^{-1} \qquad (14)$$

where δ_{rms} is the rms surface roughness, c_ℓ is the lateral crack depth, c is a constant, and c_g is a constant related to the workpiece-lap interface gap. Utilizing Equation 3b for the lateral crack depth c_ℓ and the same formalism for describing the average load per particle (P) using Equations 7-8 used for the grinding removal rate model, Equation 14 can be written in a more useful form of:

$$\delta_{rms} = \left(\frac{1}{c\sqrt{\frac{\sigma_o \pi}{f_{LF} f}} s_\ell r} + \frac{1}{\frac{r}{c_g}} \right)^{-1} \qquad (15)$$

The solid lines in Figs. 8a-b represent the roughness model as represented by Equation 15, which compare well to the experimental data for the large range of workpiece materials, abrasive sizes and grinding types. The values for σ_o, f_L, f are the same as those used for the removal rate model described in *Section A*. The values for c and c_g were best fits to the data for each grinding type (loose vs fixed). For both grinding types c_g= 6. For the loose alumina abrasive grind, c=0.4 and for the fixed abrasive diamond grind, c=1.6. Unlike with the grinding removal rate model, both the loose abrasive and fixed abrasive processes are well represented by the surface roughness model (Equation 15).

Since the abrasive size is likely the determining factor that controls the interface gap, it is not surprising that the value of c_g is the same for the various grinding process types. An important implication provided by this surface roughness model is a rule-of-thumb which shows that the rms roughness of the ground surface will not exceed the abrasive radius divided by 6 (r/c_g=$r/6$) or abrasive diameter divided by 12. For example, this model predicts that grinding with a 45 μm diameter abrasive cannot lead to a roughness greater than 3.75 μm (or 3750 nm) rms, and grinding with a 9 μm diameter abrasive cannot lead to a roughness greater than 0.75 μm (or 750 nm) rms.

Another useful insight from this model is the value of c, which essentially describes the rate at which the roughness will approach the plateau roughness as a function of lateral crack slope. The loose abrasive approaches the plateau roughness more rapidly than the fixed abrasive for the same range of the lateral crack slope. More specifically, the rate is 1.6/0.4 or 4 times faster with the loose abrasive.

The concept of the interface gap limit on the surface roughness (illustrated in Fig. 13) can be further tested by determining the surface roughness of one of the workpieces, in this case phosphate glass, which has a high s_ℓ (and is in the plateau roughness regime) as a function of applied pressure. Normally, with increase in applied pressure, the load per particle should increase and the depth of lateral cracks should increase, thereby increasing the surface roughness. However, if the roughness is now limited by the interface gap, an increase in applied pressure should have little effect on the surface roughness because the interface gap is controlled largely by the abrasive size. The results of this experiment are shown in Fig. 14, where the surface roughness did not change with increase in applied pressure, hence supporting the interface gap limit proposed in the surface roughness model. This trend has also been experimentally observed previously.[22]

5. CONCLUSIONS

An expanded grinding model to predict both material removal rate and surface roughness has been developed based on lateral crack generation. The model has been experimentally evaluated on a wide variety of workpiece materials (glasses, crystals, and glass-ceramics), grinding methods (loose and fixed), abrasive sizes (9 μm to 45 μm), abrasive types (alumina and diamond), and grinding conditions (e.g., applied pressure). This study represents an important step towards achieving a truly predictive and deterministic grinding behavior during optical fabrication.

Funding Information. U.S. Department of Energy (DE-AC52-07NA27344)

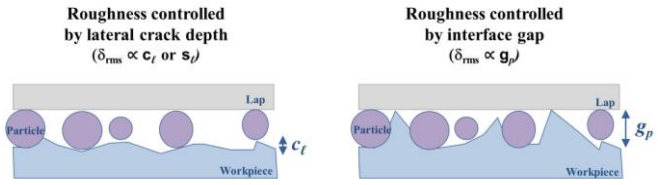

Fig. 13. Schematic illustration of the roughness model for grinding where the final roughness is controlled by the depth of lateral cracks (left) or by the interface gap between the workpiece and lap (right).

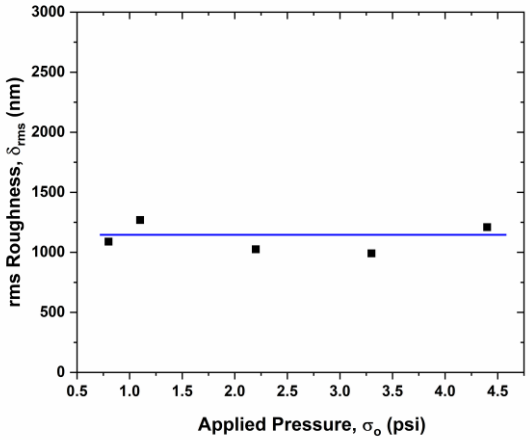

Fig. 14. rms surface roughness of phosphate glass workpiece as a function of applied pressure using loose alumina 15 μm abrasive.

References

1. T. Suratwala, *Materials Science and Technology of Optical Fabrication* (Wiley, 2018).
2. L. G. Austin, "Introduction to the mathematical description of grinding as a rate process," Powder Technology **5**, 1-17 (1971).
3. R. Klimpel and L. Austin, "The back-calculation of specific rates of breakage and non-normalized breakage distribution parameters from batch grinding data," International Journal of Mineral Processing **4**, 7-32 (1977).
4. G. Wiese and R. Wagner, "Physical model for predicting grinding rates," Appl. Opt. **13**, 2719-2722 (1974).
5. F. Aleinikov, "The effect of certain physical and mechanical properties on the grinding of brittle materials," Soviet Physics-Technical Physics **2**, 2529-2538 (1957).
6. T. Izumitani, *Optical glass*, American Institute of Physics translation series (American Institute of Physics, New York, 1986), pp. x, 197 p.
7. T. Izumitani and I. Suzuki, "Indentation hardness and lapping hardness of optical glass," Glass Technol. **14**, 35-41 (1973).
8. M. Buijs and K. Korpel-van Houten, "A model for lapping of glass," J. Mater. Sci. **28**, 3014-3020 (1993).
9. J. C. Lambropoulos, S. Xu, and T. Fang, "Loose abrasive lapping hardness of optical glasses and its interpretation," Appl. Opt. **36**, 1501-1516 (1997).
10. J. C. Lambropoulos, T. Fang, P. D. Funkenbusch, S. D. Jacobs, M. J. Cumbo, and D. Golini, "Surface microroughness of optical glasses under deterministic microgrinding," Appl. Opt. **35**, 4448-4462 (1996).
11. J. Lambropoulos, S. D. Jacobs, B. Gillman, F. Yang, and J. Ruckman, "Subsurface damage in microgrinding optical glasses," Ceram. Trans. Vol. 82, 469-474 (1997).

12. B. R. Lawn, *Fracture of brittle solids,* 2nd ed., Cambridge solid state science series (Cambridge University Press, Cambridge ; New York, 1993), pp. xix, 378 p.
13. B. Lawn and R. Wilshaw, "Indentation fracture: principles and applications," J. Mater. Sci. **10**, 1049-1081 (1975).
14. I. M. Hutchings, *Tribology : friction and wear of engineering materials* (CRC Press, Boca Raton, 1992), pp. viii, 273 p.
15. A. Arora, D. Marshall, B. Lawn, and M. Swain, "Indentation deformation/fracture of normal and anomalous glasses," J. Non-Cryst. Solids **31**, 415-428 (1979).
16. T. Suratwala, R. Steele, M. D. Feit, L. Wong, P. Miller, J. Menapace, and P. Davis, "Effect of rogue particles on the sub-surface damage of fused silica during grinding/polishing," J. Non-Cryst. Solids **354**, 2023-2037 (2008).
17. T. Suratwala, P. Miller, M. Feit, and J. Menapace, "Scratch forensics," Opt. & Photo. News **20**, 12-15 (2008).
18. T. Suratwala, L. Wong, P. Miller, M. D. Feit, J. Menapace, R. Steele, P. Davis, and D. Walmer, "Sub-surface mechanical damage distributions during grinding of fused silica," J. Non-Cryst. Solids **352**, 5601-5617 (2006).
19. T. Suratwala, M. Feit, W. Steele, L. Wong, N. Shen, R. Dylla-Spears, R. Desjardin, D. Mason, P. Geraghty, P. Miller, and S. Baxamusa, "Microscopic Removal Function and the Relationship Between Slurry Particle Size Distribution and Workpiece Roughness During Pad Polishing," J. Am. Ceram. Soc. **97**, 81-91 (2014).
20. B. Lawn, "Partial cone crack formation in a brittle material loaded with a sliding spherical indenter," Proc. R. Soc. Lond. A **299**, 307-316 (1967).
21. I. Demirci, A. Mkaddem, and D. El Khoukhi, "A multigrains' approach to model the micromechanical contact in glass finishing," Wear **321**, 46-52 (2014).
22. F. Ratajczyk, "Die Abhangigkeit des Twymaneffekts von der Dicke der abpolierten Schicht der geschliffenen Glasoberflache," Feingeratetechnik **16**, 254-256 (1967).